JGR Atmospheres

RESEARCH ARTICLE
10.1029/2020JD033696

Eastward-Propagating Planetary Waves Prior to the January 2009 Sudden Stratospheric Warming

Christian T. Rhodes[1], **Varavut Limpasuvan**[1], **and Yvan J. Orsolini**[2,3]

[1]School of the Coastal Environment, Coastal Carolina University, Conway, SC, USA, [2]Norwegian Institute for Air Research (NILU), Kjeller, Norway, [3]Department of Physics, Norwegian University of Science and Technology, Trondheim, Norway

Key Points:

- Planetary and gravity wave forcings create eastward wind maxima in the stratosphere and mesosphere before sudden stratospheric warming onset
- This double-maxima wind configuration favors planetary wave growth from wind shear instability via overreflection
- The refractive index of the wintertime middle atmosphere is conducive to the production of eastward-propagating planetary waves

Correspondence to:
C. T. Rhodes,
ctrhodes@coastal.edu

Citation:
Rhodes, C. T., Limpasuvan, V., & Orsolini, Y. J. (2021). Eastward-propagating planetary waves prior to the january 2009 sudden stratospheric warming. *Journal of Geophysical Research: Atmospheres*, *126*, e2020JD033696. https://doi.org/10.1029/2020JD033696

Received 15 AUG 2020
Accepted 19 APR 2021

Abstract Eastward-propagating planetary waves (EPWs) were investigated prior to the boreal January 2009 major sudden stratospheric warming (SSW) event simulated by the National Center for Atmospheric Research's Whole Atmosphere Community Climate Model with specified dynamics. About 22 days before SSW onset, a background flow with jet maxima around the upper polar stratosphere and subtropical mesosphere developed due to the net forcing by gravity and planetary waves. The mesospheric wind structure was largely unstable and supported a wave geometry conducive to overreflection. With a zonal phase speed of ~10 m s^{-1}, EPWs appeared near their turning and critical layers as wavenumber-2 perturbations in the stratosphere and mesosphere. Accompanied by upward EPW activity from the lower stratosphere, EPW growth exhibited characteristics of wave instability and overreflection.

1. Introduction

The wintertime structure of the stratosphere and mesosphere arises from the competing effects between net radiative heating and wave forcing (Andrews et al., 1987). The main source of stratospheric variability is upward-propagating planetary waves (PWs) generated in the troposphere by large-scale orography and heat sources (e.g., Charney & Eliassen, 1949; Smagorinsky, 1953). During the Northern Hemisphere (NH) winter, the prevailing eastward flow of the polar night jet allows PWs to propagate into the stratosphere and, upon their dissipation, impact the flow. Above the stratosphere, gravity waves (GWs) from tropospheric sources impose a strong westward drag on the eastward flow, capping the top of the polar night jet and affecting the polar stratopause (Duck et al., 2001; C. Leovy, 1964). While PWs and GWs can modulate one another by altering the background temperature and wind, their combined influence keeps the polar vortex warmer than otherwise under radiative equilibrium.

Occasionally, when the upward PW activity is large, its eventual dissipation in the NH winter polar stratosphere can cause the zonal-mean zonal wind, $\overline{u}$, to reverse direction as the polar region undergoes rapid warming (Matsuno, 1971), resulting in a phenomenon called a major sudden stratospheric warming (SSW). Occurring roughly 60% of NH winters (e.g., Butler et al., 2015), SSWs are also characterized by the perturbed stratospheric polar vortex becoming split (i.e., split SSW) or greatly displaced off the North Pole (i.e., displacement SSW). The impacts of SSWs have been linked to anomalously cold conditions over Europe and Northeast America (e.g., Baldwin & Dunkerton, 2001) and atypical atmospheric perturbations above the stratosphere (Goncharenko et al., 2010; Pedatella et al., 2016; Sassi et al., 2016; Zhang et al., 2021).

The $\overline{u}$ structure in the stratosphere and mesosphere can exhibit regions of unusually strong wind shear. There, the flow can become barotropically and/or baroclinically unstable, leading to the appearance of unstable PWs (e.g., Dickinson, 1973; C. B. Leovy & Webster, 1976; Matthias & Ern, 2018). For $\overline{u}$ to be unstable, the generally positive meridional quasi-geostrophic (QG) potential vorticity (PV) gradient ($\overline{q}_\phi$) associated with the wintertime circulation must become negative (e.g., Salby, 1996). To serve as a source for an unstable PW of a certain zonal phase speed, c_x, that region must also contain a critical layer where $\overline{u}$ matches c_x (Dickinson, 1973). Hartmann (1983) used a linear barotropic model and a QG baroclinic model to examine instabilities of the eastward stratospheric polar night jet. He found that, when the instability was seated on the poleward flank of the jet, the most unstable modes were wavenumbers 1 and 2 with periods of a few days. When the instability was seated on the midlatitude flank of the jet, the most unstable modes were wavenumbers 1–3 with periods of a week or more. Manney et al. (1988) suggested that these periods are

likely slightly longer in observations since the nonlinear effect of instability tends to weaken and broaden the jet (Pedlosky, 1987).

Using a fully nonlinear nondivergent barotropic model, Orsolini and Simon (1995) simulated the generation and life cycle of PWs arising from an unstable polar night jet as well as those from an unstable double jet meridional profile. These authors found similar low-wavenumber unstable modes as Hartmann (1983) with periods on the order of days for the single jet case. Planetary-scale vortices developed to expel the low PV air on the poleward flank of the jet into lower latitudes, acting to remove the sign reversal of $\overline{q}_\phi$. In addition to low-wavenumber disturbances, eddies of higher wavenumbers (3–4) were found in the double jet case. Although perturbations of higher wavenumbers have larger growth rates, Hartmann (1983) suggested that low-wavenumber instabilities (given the predominance of low-wavenumber disturbances in the stratosphere that could seed the unstable waves) would be more likely than those of higher wavenumbers to derive energy from an unstable flow.

Prior to the split SSW of January 2009, a few studies noted the presence of slow eastward-propagating PWs, hereafter EPWs, in the mesosphere (Coy et al., 2011; Iida et al., 2014; Song et al., 2020). Using a high-top forecast model with data assimilation, Coy et al. (2011) suggested that these mesospheric EPWs directly propagated from the troposphere with the underlying bursts of wavenumber-2 PW activity prior to the SSW onset and their eventual dissipation in the lower mesosphere. Using satellite observations, Iida et al. (2014) instead suggested that the EPW appearance before SSW onset could be generated *in situ* by shear instability of the polar night jet. Based on reanalyses, Song et al. (2020) demonstrated that the amplification of wavenumber-2 EPW before the 2009 SSW onset is likely attributed to GW forcing in the upper stratosphere and lower mesosphere.

Regardless of their source, EPWs may be a common feature, particularly during periods leading up to SSW. In the composite study of Limpasuvan et al. (2016) based on 13 SSW events, a robust signature of zonal wavenumber-1 EPW with an eastward period of around 10 days was evident between 40 and 60 km and over the polar region, intensifying roughly 10 days before SSW onset (see their Figure 9). However, these authors did not discuss the cause of the wave presence and focused only on the wavenumber-1 westward-traveling wave that developed after the SSW onset. Hence, the exact nature of EPWs and why they occur before SSW onset remain unclear. Using a high-resolution global circulation model (GCM) integrated over 3 years, Sato and Nomoto (2015) suggested that EPWs may be generated by baroclinic instability in the mesosphere.

In general, propagating PWs can interact with a preexisting unstable region where the wave first becomes evanescent (i.e., its amplitude diminishes exponentially with height). This effect allows for "wave tunneling" as the perturbation extends beyond the wave propagation region. If a wave is able to tunnel to its critical layer, then wave growth can occur. This stimulated emission may be conceptualized through overreflection (Harnik & Heifetz, 2007). Following Lindzen et al. (1980), Figure 1 illustrates overreflection for a simplified atmosphere with some assumed $\overline{u}$ vertical profile. Overreflection occurs when an incident PW reflects from the unstable or evanescent region with more energy than it initially had (thick arrow). The turning level is indicated by a $\overline{q}_\phi$ sign change and physically represents the layer at which wave disturbances begin to break or become unstable. An upward-propagating incident PW can tunnel through the evanescent region before eventually reaching the critical layer. An associated transmission occurs when the diminished PW (dashed arrow) emerges from the critical layer with more energy than the incident PW within the evanescent region. From this perspective, a wave generated from shear instability can manifest as an overreflected component, emanating downward from the turning level, as well as a transmitted component, emerging from the critical layer (Dickinson, 1973). If the evanescent region is sufficiently thin, the exponentially decaying waves can readily reach the critical layer via tunneling.

To provide a detailed account of the dynamics leading up to SSW onset, the present study examines mesospheric EPWs prior to the 2009 SSW using a high-top GCM constrained by reanalysis below 50 km. The evolution of the background flow conditions supporting EPW is explored through the interplay of GWs and PWs. We identify a similar double $\overline{u}$ maxima in the meridional direction, as noted by Orsolini and Simon (1995). In fact, this wind configuration consists of well-separated and strengthened subtropical mesospheric and polar night jets. The strong shear instability between the two jet cores promotes the growth of unstable EPWs whose characteristics are consistent with wave overreflection. To our knowledge, this is the

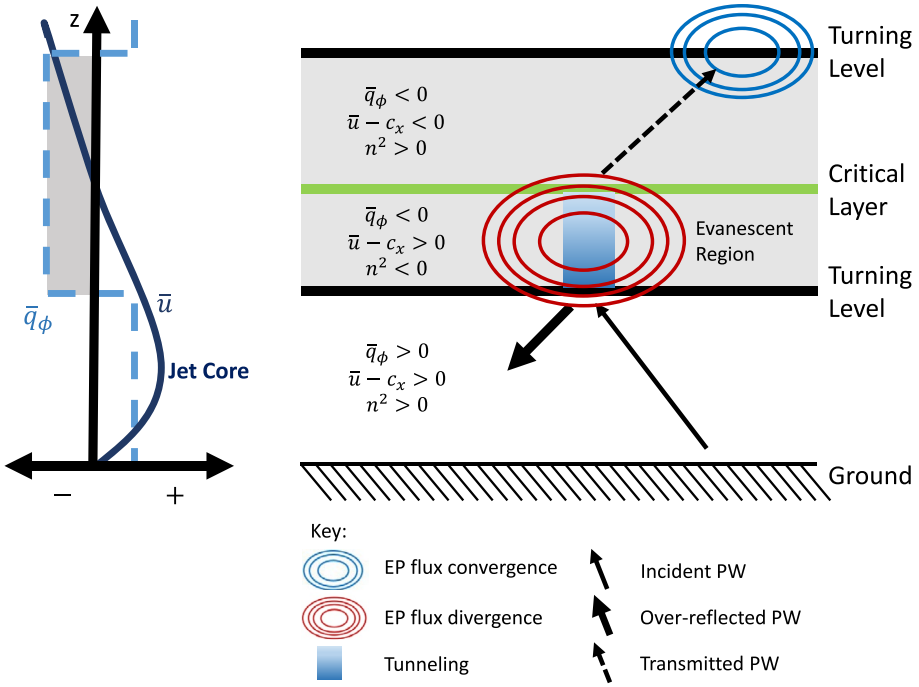

Figure 1. A schematic of planetary wave (PW) overreflection with background $\bar{u}$ and $\bar{q}_\phi$ fields shown on the left with arbitrary magnitudes. On the right, upward-propagating PWs (thin solid arrow) overreflect at the turning level, resulting in a reflected wave (thick solid arrow) with enhanced energy. Tunneling to the critical layer is represented by a light blue gradient. A transmitted wave (thin dashed arrow) appears above the critical layer. Gray shading indicates the negative $\bar{q}_\phi$ region.

first study to examine the mesospheric instabilities prior to an SSW event from the perspective of overreflection. Our study may lead to a better understanding of mesosphere–stratosphere coupling and help assess the role of the mesosphere in SSW predictability.

2. Methods

2.1. Model

We utilized the Whole Atmosphere Community Climate Model, Version 4 (WACCM) developed at the National Center for Atmospheric Research. As part of the Community Earth System Model Version 1.2, WACCM is an atmosphere-only global chemistry–climate model that extends up to ~145 km. Details of WACCM are provided by Marsh et al. (2013). Notable model features include parameterization of GW drag (GWD) generated by convection and fronts as well as mountain stresses which have improved the frequency of SSWs (Richter et al., 2010).

WACCM was run in the specified dynamics configuration from 1980 to 2013. This configuration has a horizontal resolution of 0.95° latitude by 1.25° longitude, 88 vertical levels, and key dynamical variables output daily. The model's temperature and dynamics are constrained up to 50 km with six-hourly Modern-Era Retrospective Analysis for Research and Application Version 2 reanalysis (Gelaro et al., 2017). A linear transition is applied between the nudged output below 50 km and the overlying (fully interactive) free-running region above 60 km.

2.2. SSW Identification and Classification

We identified SSW events using the criteria of Limpasuvan et al. (2016). Based on the zonal-mean zonal wind and temperature averaged between 70°N and 90°N during the extended winter (October–April inclusively), an SSW occurs when (1) the temperature falls below 190 K between 80 and 100 km, (2) the zonal

wind reverses from eastward to westward at 1 hPa and persists longer than 5 days, and (3) the stratopause altitude based on the zonal-mean temperature maximum between 20 and 100 km exhibits a vertical discontinuity of at least 10 km. These criteria in particular select SSWs with elevated stratopauses during which the vortex recovery is accompanied by a newly reformed stratopause much above its climatological altitude (Manney et al., 2008). These SSWs capture the strong coupling between the upper stratosphere and the mesosphere–lower thermosphere during SSWs which is pertinent in this study. We identified 13 ES-SSW events in our simulations between 1980 and 2013. In YYYYMMDD format, the onset dates of these ES-SSWs are 19840221, 19841230, 19870122, 19890219, 19950127, 19971223, 20020213, 20031220, 20060109, 20090122, 20100124, 20120113, and 20130105. We emphasize that the SSW onset is defined based on $\overline{u}$ at 1 hPa reversing direction. While the current study focuses on the 2009 event, winters when other SSW events occurred are removed from the climatology of quiet, non-SSW winters.

2.3. Data Analyses and Diagnostics

Fourier transform was performed with a sliding 31-day Hanning window, allowing for subseasonal variations. A band-pass filter over desired zonal wavenumbers and phase speeds was used to elucidate various PWs. Following Coy et al. (2011), the presence of a wave with a specific zonal wavenumber was detected if the geopotential height perturbation (GHP) amplitude exceeded 200 m. After binning the geopotential height amplitude by zonal phase speed, the mean phase speed and standard deviation were calculated. A critical layer was identified if $\overline{u}$ was within 0.05 standard deviations of the mean phase speed and the GHP amplitude exceeded 200 m.

The Eliassen-Palm (EP) flux was computed using formulation associated with the transformed Eulerian-mean (TEM) equations given in Andrews et al. (1987). The EP flux vector is expressed as $\boldsymbol{F} \equiv \left(0, F^{(\phi)}, F^{(z)}\right)$ such that

$$F^{(\phi)} \equiv \rho_0 R_e \cos\phi \left(\frac{\partial \overline{u}}{\partial z} \overline{v'\theta'} \left(\frac{\partial \overline{\theta}}{\partial z} \right)^{-1} - \overline{v'u'} \right) \tag{1a}$$

$$F^{(z)} \equiv \rho_0 R_e \cos\phi \left[\left(f - \left(R_e \cos\phi \right)^{-1} \frac{\partial \overline{u} \cos\phi}{\partial \phi} \right) \overline{v'\theta'} \left(\frac{\partial \overline{\theta}}{\partial z} \right)^{-1} - \overline{w'u'} \right] \tag{1b}$$

where ϕ is the latitude, z is the log-pressure height, ρ_0 is the reference density, R_e the Earth's radius, f is the Coriolis parameter, and θ is the potential temperature. The zonal, meridional, and vertical velocities are represented by u, v, and w, respectively. Overbars and primes represent the zonal mean and perturbation, respectively. For these calculations, 5-day running averages were applied to the dependent field variables (wind, temperature, etc.) to remove perturbations with periods <5 days (or with $c_x > 46$ m s^{-1} at 60°N). The EP flux represents the product of the wave group velocity and the wave activity density (Andrews et al., 1987). The second term in parentheses on the right-hand side of Equation 1a is dominant and represents the northward eddy momentum flux. The first term in brackets on the right-hand side of Equation 1b is dominant and indicates the northward eddy heat flux. The divergence of EP flux $(\nabla \cdot \boldsymbol{F})$ is the northward eddy flux of PV. In a region of positive meridional PV gradient (as is the typical case in the middle atmosphere), the wave group velocity is parallel to the EP flux vector. In the NH, EP flux divergence (convergence) corresponds with a decrease (increase) in wave activity and/or an eastward (westward) acceleration on the background wind.

GWD is determined as the sum of parameterized and resolved zonal GWD. The resolved zonal GWD was estimated as the EP flux divergence for perturbations of zonal wavenumbers greater than 6 (e.g., Fetzer & Gille, 1994).

The meridional QG PV gradient in spherical coordinates or $\overline{q}_\phi$ (e.g., as defined in O'Neill & Youngblut, 1982) was calculated based on 5-day running averages of dependent field variables. By definition,

$$\overline{q}_\phi = 2\Omega\cos\phi - R_e^{-1}\frac{\partial}{\partial\phi}\left(\frac{1}{\cos\phi}\frac{\partial\left(\overline{u}\cos\phi\right)}{\partial\phi}\right) - \frac{R_e f^2}{\rho_0}\frac{\partial}{\partial z}\left(\frac{\rho_0}{N_B^2}\frac{\partial\overline{u}}{\partial z}\right) \quad (2)$$

where $N_B \equiv g\,\partial\ln\left(\theta\right)/\partial z$ is the Brunt-Väisälä (or buoyancy) frequency, Ω is the Earth's angular frequency, and g is gravity. In later discussion, we refer to the positive definite first term on the right-hand side as the "beta term" associated with the meridional gradient of f, the second term as the "barotropic term" associated with horizontal wind curvature, and the third term as the "baroclinic term" associated with the vertical wind curvature.

By imposing a wave solution on geopotential perturbations in the linearized QG PV equation (not shown), a Helmholtz equation is obtained with the squared refractive index ($\boldsymbol{n^2}$) as an eigenvalue (Andrews et al., 1987). The $\boldsymbol{n^2}$ field can be diagnosed to illuminate how PWs of certain zonal wavenumbers (s) and c_x propagate in $\overline{u}$ (Andrews et al., 1987). Its formulation is given as

$$n^2 = \frac{\overline{q}_\phi}{R_e\left(\overline{u} - c_x\right)} - \left(\frac{s}{R_e\cos\phi}\right)^2 - \left(\frac{f}{2N_B H}\right)^2 \quad (3)$$

where H is the scale height. PWs tend to propagate toward a large positive refractive index and are unable to propagate in regions of negative index. At a critical layer where $\overline{u} - c$ is zero, $\boldsymbol{n^2}$ is infinity and attracts PWs. At a turning level, $\boldsymbol{n^2}$ decreases to zero and discourages PW propagation into this region. Since the second and third terms on the right-hand side of Equation 3 are positive definite, a sign change in $\overline{\boldsymbol{q}}_\phi$ implies a sign change in $\boldsymbol{n^2}$ and indicates the existence of a turning level. In the figures below, $\overline{\boldsymbol{q}}_\phi$ and $\boldsymbol{n^2}$ are nondimensionalized by Ω and R_e^2, respectively.

3. The 2009 SSW Event

3.1. Formation of a Double-Maxima Wind Configuration

With an onset date of January 22, the 2009 split SSW event was associated with a very strong polar warming of more than 50 K in a matter of days (e.g., Harada et al., 2010). Evident in Figure 2a (showing the $\overline{u}$ evolution at 60°N), the upper-mesospheric eastward flow reversed ~5 days prior to the onset date, indicated by the vertical dashed line. The early reversal of the upper-mesospheric wind before SSW onset is also evident in the NASA Microwave Limb Sounder (MLS) observations of Iida et al. (2014). In the stratosphere and lower mesosphere, the polar jet strengthened a few days prior to wind reversal.

The $\overline{u}$ meridional cross sections prior to the onset are compared to the December–February (DJF) climatology in Figures 2b–2d. Here, the wind climatology excludes years containing ES-SSWs with onset dates listed in Section 2.2. On December 25 (corresponding to the gold vertical line in Figure 2a), the wind structure was similar to climatology (Figure 2d), with a single maximum near the midlatitude stratopause. The eastward wind magnitude was, however, stronger than climatology. A few days later (on December 31 corresponding to the brown vertical line in Figure 2a), the wind structure departed significantly from climatology, consisting of two local maxima of comparable strength (Figure 2c). One maximum appeared in the subtropical upper mesosphere and the other corresponded to a strengthened polar night jet. Iida et al. (2014) reported a similar double-maxima wind configuration before the 2009 SSW onset in MLS observations.

3.2. Interplay of PWs and GWs

The rapid wind evolution between December 25 and 31 was investigated with respect to PW forcing (corresponding to disturbances of zonal wavenumbers 1–6) and GWD (described in Section 2.3) on the background wind (Figure 3). On December 25, PW activity was weak with the expected upward and equatorward propagation through the region of eastward wind from the midlatitude lower stratosphere to low-latitude upper mesosphere (Figure 3a). Nevertheless, upward PW activity appeared in the upper region of the polar night jet and its EP flux convergence led to a westward forcing (blue contour) of around 10 m s^{-1} day^{-1}.

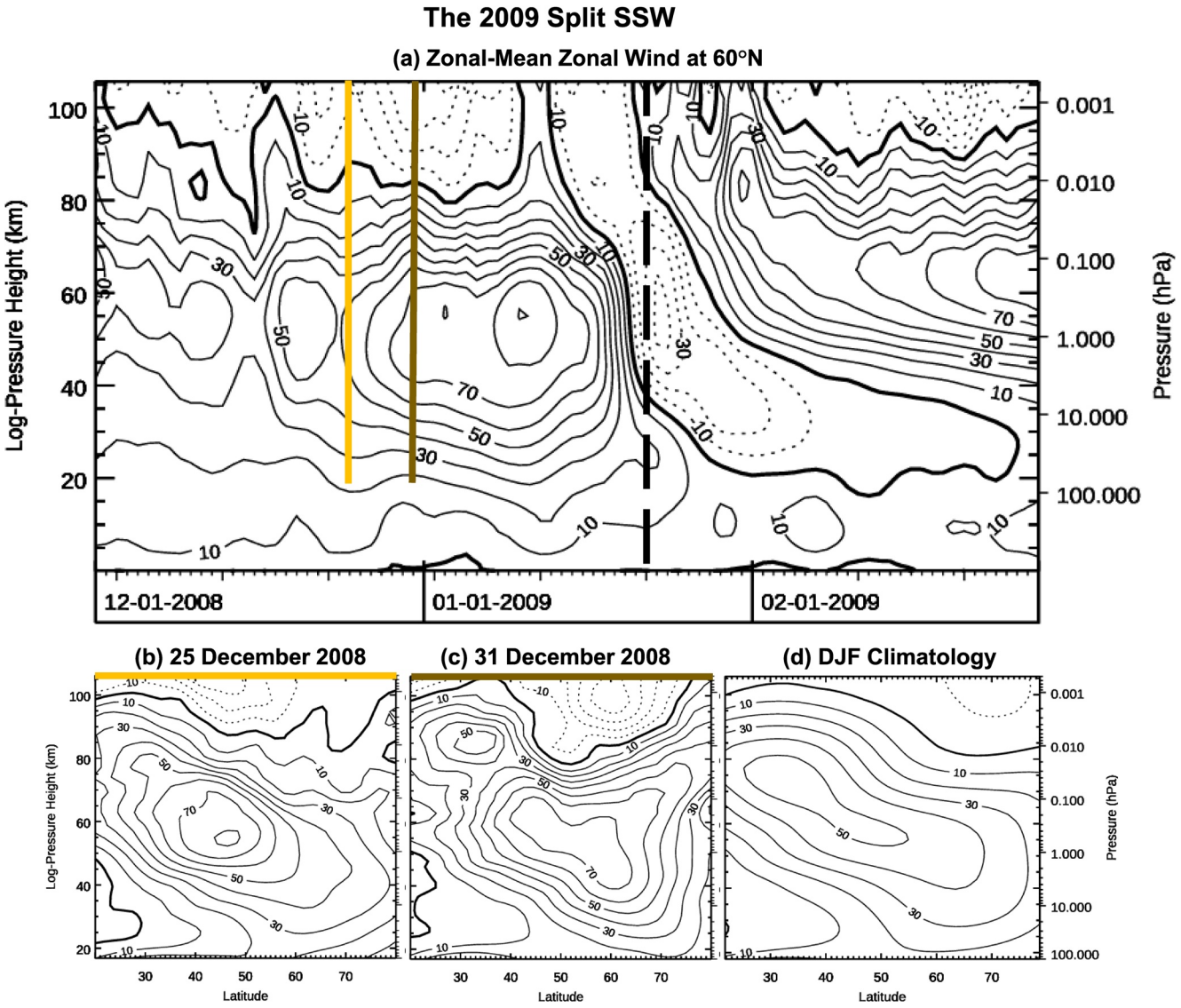

Figure 2. (a) Altitude–time evolution of $\overline{u}$ at 60°N during the 2009 split SSW event with an onset date of January 22 as indicated by a vertical dashed line. Westward (dotted black contour) and eastward (solid thin black contour) wind increment by 10 m s^{-1}, with the zero-wind line thickened. (b–d) Altitude–latitude sections of $\overline{u}$ for (b) December 25, 2008, (c) December 31, 2008, and (d) the December–February climatology for 1980–2013 (excluding years with SSWs listed in Section 2.2). SSW, sudden stratospheric warming.

By December 31, PW activity greatly intensified, penetrating well into the subtropical mesosphere before damping. Centered near 35°N and 80 km, the EP flux convergence exerted strong westward forcing in excess of 60 m s^{-1} day^{-1} between the subtropical and polar jet cores.

Figures 3c and 3d illustrate the corresponding GWD. On December 25, when $\overline{u}$ was similar to climatology, strong westward GWD (blue contours) capped the top of the eastward jet below the zero-wind line (bold black contour). The forcing was most prevalent around 80 km between 30°N and 50°N. Such a GWD pattern was due to westward GWs that were allowed to reach the mesosphere by the strong eastward wind below 60 km. With the development of the double-maxima wind configuration on December 31, eastward GWD (red contours) became more apparent. Wintertime PWs propagating upward from the troposphere broke along the edge of the polar jet, as suggested by the EP flux pattern in Figure 3b, and exerted a westward acceleration along the equatorward flank of the polar vortex below 70 km. The resultantly weakened eastward wind allowed eastward GWs to reach the mesosphere and impose an eastward $\overline{u}$ tendency near the subtropical mesospheric jet core, evident in Figure 3d. GWD also became increasingly westward in the midlatitudes

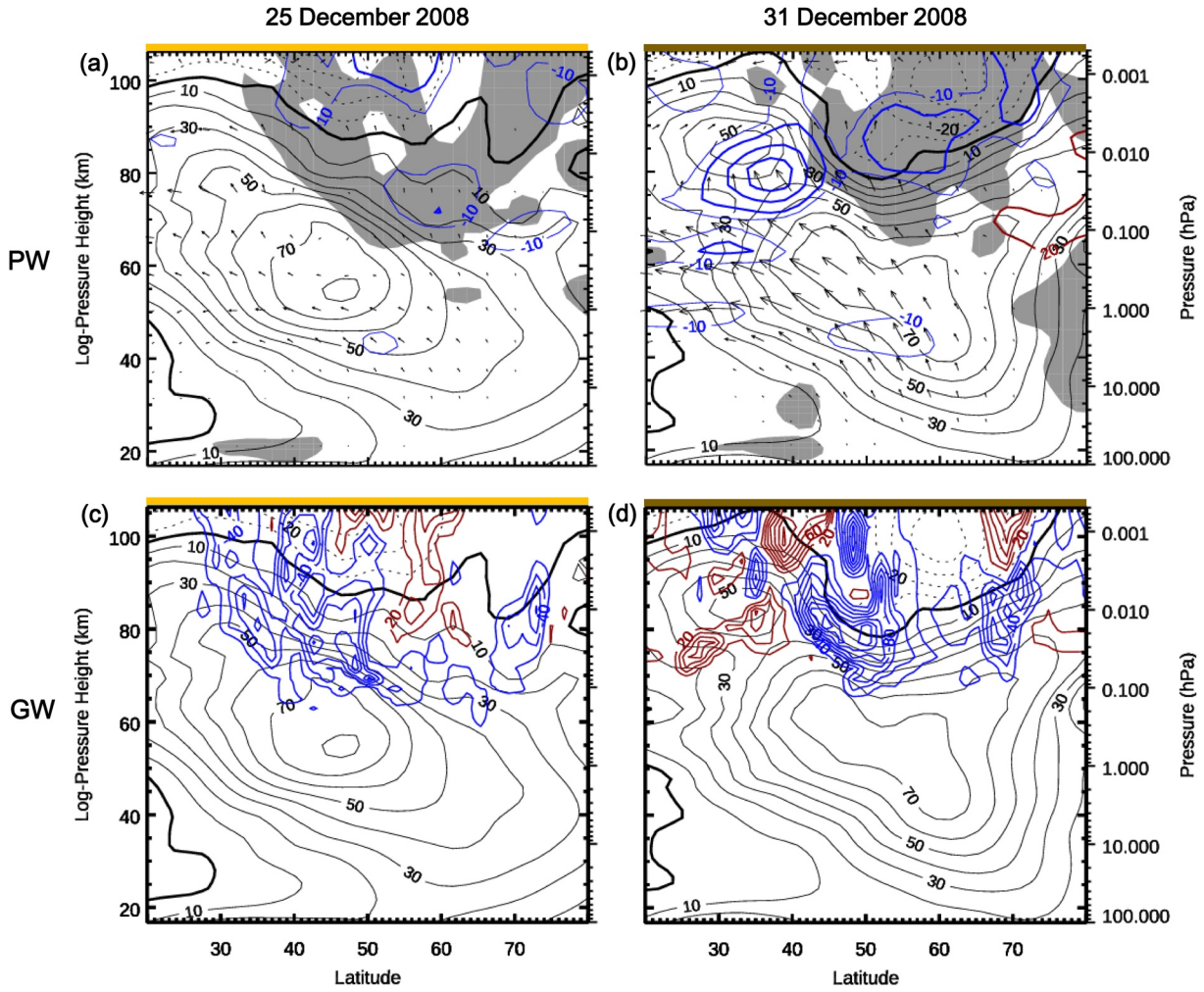

Figure 3. Altitude–latitude sections of (a, b) PW EP flux and its divergence and (c, d) GWD (resolved and parameterized) during December 25 and December 31, 2008. Westward (dotted black contour) and eastward (solid thin black contour) winds increment by 10 m s^{-1}, with the zero-wind line thickened. Incremented by 20 m s^{-1} day^{-1}, GWD and PW EP flux divergence are contoured in blue for westward forcing and red for eastward forcing. For (a) and (b), the 10 m s^{-1} day^{-1} isopleth is indicated by the thin blue contour to illustrate the broad extent of PW forcing. The meridional EP flux vector component was scaled by $\left(100\pi R_e\rho_0\right)^{-1}\cos\phi$ and the vertical component by $\left(R_e\rho_0\right)^{-1}\cos\phi$. Gray shading indicates regions of negative $\overline{q}_\phi$. PW, planetary wave; EP, Eliassen-Palm; GWD, gravity wave drag.

(with values exceeding 60 m s^{-1} day^{-1}) and concentrated near the zero-wind line. Such strong decelerative effects increased the wind shear as indicated by the constricted isotachs.

Figure 4 shows the latitude–time evolution of PW forcing and GWD (both as filled contours) averaged between 0.2 and 0.02 hPa. This pressure range is where strong GWD appears in Figures 3c and 3d. We overlaid the eastward $\overline{u}$ averaged between 1.0 and 0.1 hPa as dotted line contours to capture the evolution of the polar night jet in the upper stratosphere (e.g., see Figures 2b and 2c). To illustrate the evolution of subtropical mesospheric jet, we also superimposed eastward $\overline{u}$ averaged between 0.1 and 0.01 hPa in solid line contours. For clarity, only eastward wind values of 30 m s^{-1} and greater are shown.

At this altitude range, we clearly see that, equatorward of 50°N, westward PW forcing maximized after December 25 (indicated by the gold vertical line), consistent with the transition between Figures 3a and 3b. Strong westward PW forcing then appeared over the entire NH just before SSW onset (indicated by the vertical dashed line). Seen in Figure 4b, strong westward GWD (blue regions) persisted over the polar jet and followed the jet's migration northward. Upon SSW onset, eastward GWD eventually dominated throughout the NH due to the underlying stratospheric wind reversal, as observed by De Wit et al. (2014).

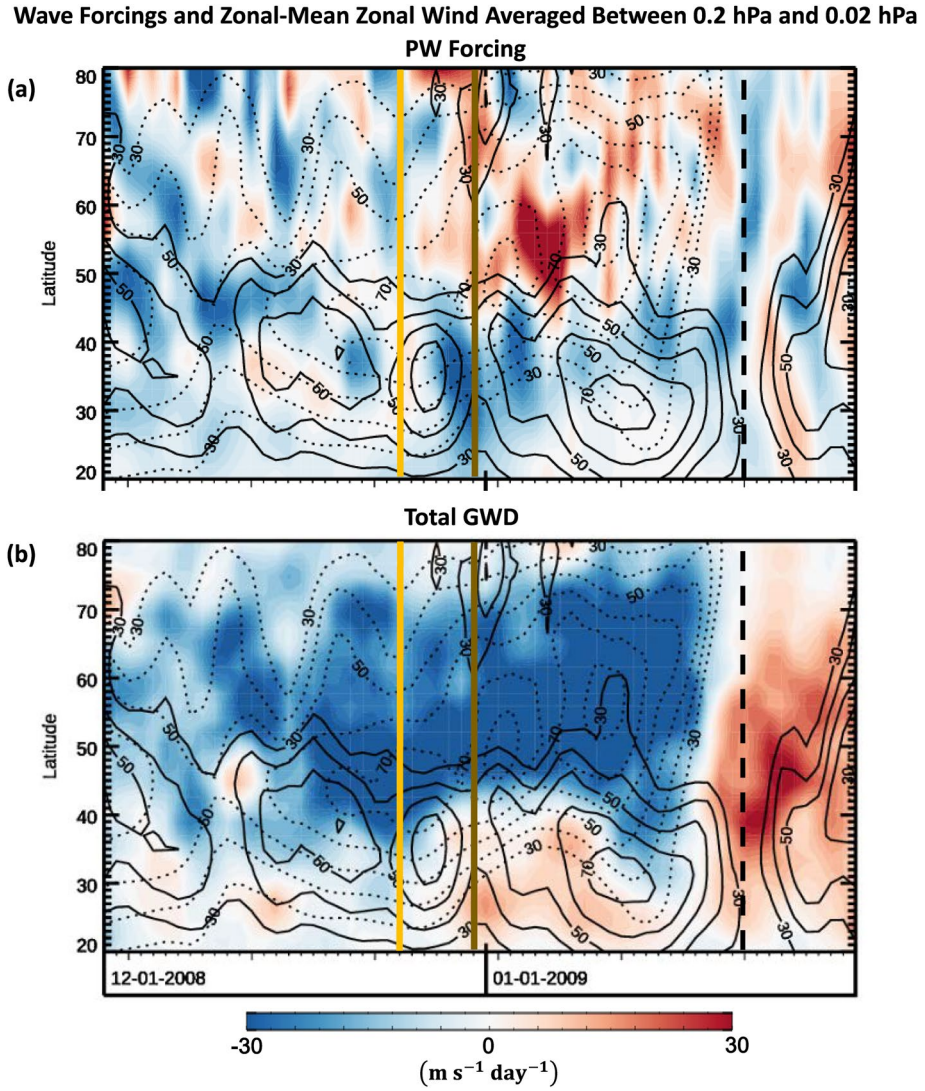

Figure 4. Latitude–time evolution (averaged between 0.2 and 0.02 hPa) showing (a) PW forcing and (b) GWD, both in m s^{-1} day^{-1}. Eastward $\overline{u}$ (m s^{-1}) values averaged from 1.0 to 0.1 hPa outline the polar jet (dotted contours). Eastward $\overline{u}$ values averaged from 0.1 to 0.01 hPa outline the subtropical jet (solid contours). Vertical gold and brown lines mark December 25 and 31, 2008, respectively. The latter date corresponds to the formation of a double-maxima wind structure. The dashed vertical line indicates SSW onset on January 22, 2009. PW, planetary wave; GWD, gravity wave drag; SSW, sudden stratospheric warming.

By December 31 (brown vertical line), the formation of the double-maxima wind configuration noted in Figures 2 and 3 commenced as the polar jet migrated poleward. Concurrently, the westward PW forcing and eastward GWD both peaked around 30°N between the subtropical jet and the polar jet. Comparing Figures 3b and 3d near 80 km and equatorward of 40°N, the eastward GWD (red contours) exceeded the westward PW forcing (blue contour). The resulting net eastward forcing (from GWs and PWs) helped to maintain the subtropical mesospheric jet core. The nearby westward PW forcing maxima between the subtropical and polar jets slowed the local eastward wind between the jet cores. To this end, GWD and PW forcing conspired to form the double-maxima wind configuration. In their model simulation, Sato and Nomoto (2015) identified similar interplay between GWD and PW forcing in the formation of the double-maxima wind configuration (see their Figures 3 and 4).

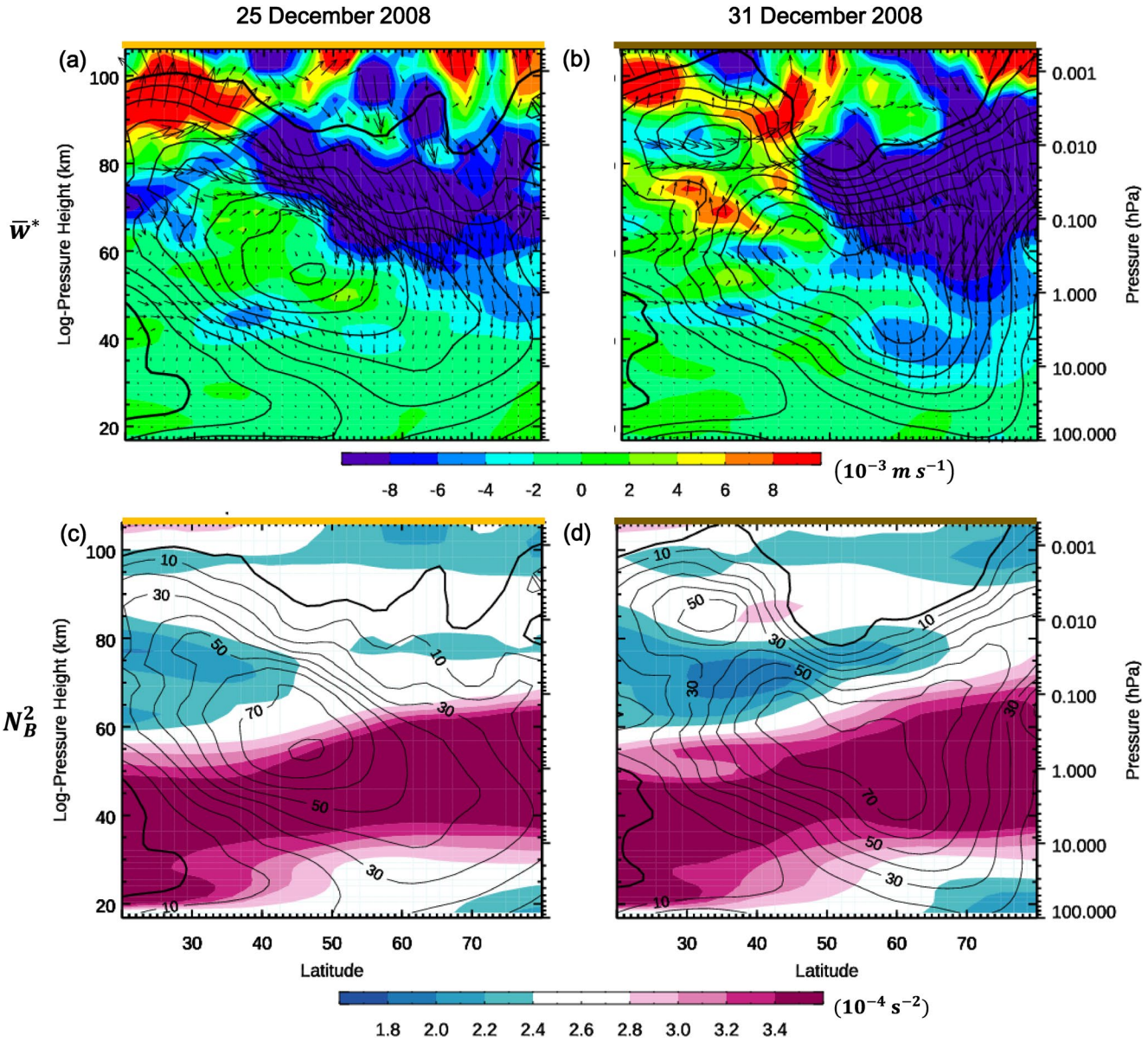

Figure 5. Altitude–latitude sections of (a, b) $\overline{w}^*$ and (c, d) N_B^2 as shading. (a, b) The residual circulation vectors ($\overline{v}^*$, $\overline{w}^*$), multiplied by (1, 1,000), are overlaid. Only eastward $\overline{u}$ is shown and contoured every 10 m s^{-1} as thin black contours. The zero-wind line is thickened.

3.3. Static and Shear Instabilities

In Figures 3a and 3b on December 25 and 31, a region of negative $\overline{q}_\phi$ exists below the zero-wind line suggesting a configuration in which the turning level lies below the critical layer, similar to the idealized schematic in Figure 1. Therefore, a preexisting configuration was available to support overreflection given the introduction of sufficient incident PW activity and/or instability.

From the TEM perspective, net wave forcing drives a (residual) mean meridional circulation, ($\overline{v}^*$, $\overline{w}^*$), to help maintain thermal wind balance. Here, $\overline{v}^*$ and $\overline{w}^*$ represent the meridional and vertical motion, respectively. Figures 5a and 5b show the mean meridional circulation as vectors for December 25 and 31. On December 25, the poleward motion corresponded with westward GWD (seen in Figure 3c) and, by continuity, resulted in strong downward motion over the polar region (Figure 5a). As highlighted by the negative $\overline{w}^*$ region (cool-colored shading), such downwelling extended largely across the NH between 60 and 90 km

and corresponds to a well-documented wintertime phenomena driven by GWD that helps maintain the stratopause (e.g., Hitchman et al., 1989). With the formation of the double-maxima wind configuration (Figure 5b), upwelling (warm-colored shading) replaced downwelling around 30°N–50°N and 60–80 km as eastward GWD became dominant near the subtropical mesospheric jet core.

Anomalous upwelling can lead to adiabatic cooling and affects (vertical) static stability by altering the vertical temperature gradient. Illustrating N_B^2, Figure 5c reveals that static stability between 60 and 90 km tended to be weak (blue shading) equatorward of 40°N. By December 31 (Figure 5d), the strong upwelling identified in Figure 5b led to extensive cooling and, consequently, widespread areas of weakened static stability between the subtropical mesospheric and polar jets of the double-maxima wind configuration.

The baroclinic term of $\overline{q}_\phi$, defined in Equation 1, depends on N_B^2 and the vertical wind shear. The diminished static stability and enhanced vertical wind shear would increase the contribution from the baroclinic term and reduce the overall $\overline{q}_\phi$, assuming other terms in Equation 1 are fixed. Comparing Figures 5c and 5d near 55°N and 80 km, we note that a strong vertical wind shear (evidenced by the tightened isotachs) coincides with an area of drastic N_B^2 decline. With the development of a double-maxima wind structure, we would expect $\overline{q}_\phi$ to decrease.

Figure 6 illustrates the relative contribution of various terms to $\overline{q}_\phi$ in Equation 1. Positive and negative (nondimensionalized) $\overline{q}_\phi$ values are shown in Figures 6a–6c. The negative $\overline{q}_\phi$ region is bounded by gray shading and corresponds to the gray shading in Figures 3a and 3b. In Figures 6d–6f, regions where the magnitude of the beta, barotropic, or baroclinic term in Equation 2 dominates over other terms are shaded in blue, gray, or red, respectively. Light and dark tints of each color indicate whether the term is contributing positively (light) or negatively (dark) to $\overline{q}_\phi$. For example, since the planetary vorticity term is always positive, the dominance of the beta term is always represented as a light blue.

With the development of the double-maxima wind configuration in Figures 6b and 6c, increased positive $\overline{q}_\phi$ values developed into well-organized cores (brown-shaded contours), nearly collocated with the local wind maxima. Figures 6e and 6f show that the enhanced values were dominated by the barotropic term (gray region), indicating a strong horizontal wind curvature. The increased curvature is attributed to the strong westward GWD near the zero-wind line and the adjacent eastward GWD (see Figure 3d), as well as the pronounced westward PW forcing in the subtropics. A valley of low $\overline{q}_\phi$ developed between the local maxima extending diagonally from the poleward side of subtropical jet near 80 km. Regions of negative $\overline{q}_\phi$ (gray- and purple-shaded contours) increased in magnitude on December 31 and, approaching onset, peaked above the zero-wind line near 80 km and 50°N. Sato and Nomoto (2015) found a decrease in their modified PV gradient that coincided with N_B^2 decline (attributed also to upwelling and adiabatic cooling) in a similar location between jet cores.

Given the split nature of the 2009 SSW, we investigate the evolution of the wavenumber-2 GHP amplitude (averaged between 45°N and 55°N) as a function of zonal phase speed and time at various altitude levels in Figure 7. Following the formation of the double-maxima wind configuration on December 31 (marked by the brown vertical line), the wavenumber-2 GHP amplitude with a mean eastward phase speed appeared over a deep layer between 1 and 0.1 hPa. About 10 days before SSW onset, the wavenumber-2 peaked near 5 m s^{-1}. Iida et al. (2014) observed very similar slow EPWs associated with the double-maxima wind configuration in observations. A similar shift toward the dominance of slow eastward phase speed for PWs was also noted in Sato and Nomoto (2015).

The presence of unstable EPW arising from the reversal of PV is further suggested by the nonzonally averaged view of the circulation. Figure 8 illustrates the carbon monoxide (CO) distribution (as filled contours) at 0.1 hPa. At this altitude, CO serves as a nearly conservative tracer that mimics PV (e.g., Solomon et al., 1985). Overlaid on this figure are geopotential height (black) contours, outlining the polar vortex. On December 31 (Figure 8a), a wavenumber-1 perturbation appeared as the polar vortex shifted off the pole, increasing the local zonal wind near the International Date Line. By January 6 (Figure 8b), the vortex further deformed with features indicative of PW breaking, and an irreversible mixing, along the vortex's edge. A filament of low-CO bluish air (and high PV, not shown) was advected equatorward around 30°N, just poleward of the subtropical jet. This filament structure illustrates the local meridional gradient reversal of

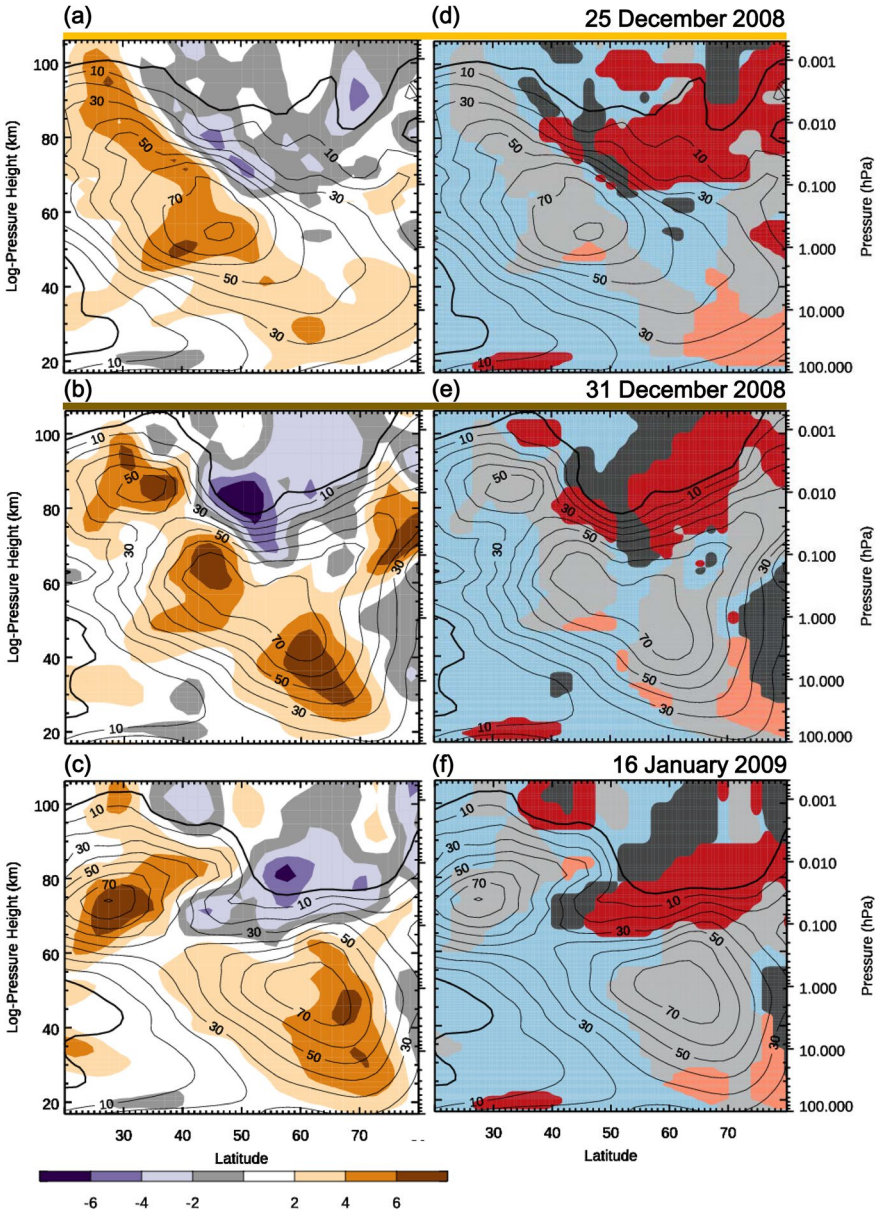

Figure 6. Altitude–latitude sections of (a–c) nondimensionalized $\overline{q}_\phi$ and (d–f) the dominant terms contributing to $\overline{q}_\phi$. Dates are shown at the upper right of each row. (d–f) In reference to the right-hand side of Equation 1, blue-, gray-, and red-shaded regions indicate the dominance of the first, second, and third term, respectively. Dark (light) colors represent a negative (positive) contribution to $\overline{q}_\phi$. Eastward $\overline{u}$ is contoured every 10 m s^{-1} as thin black contours, with the zero-wind line thickened.

PV that destabilized the flow. Finally, by January 16, the CO distribution was dominated by a wavenumber-2 pattern as a result of two partially separated low-pressure systems. This pattern migrated slowly eastward thereafter, as suggested by Figure 7c.

As seen in Figure 7, the presence of wavenumber-2 EPWs persisted up to SSW onset. This persistence coincides well with the lingering presence of the double-maxima wind configuration shown in Figure 4. Between January 25 December and 22, the subtropical mesospheric core (solid contour in Figure 4) and the polar jet core (dotted contours) intensified as the latter continued to migrate poleward. We identified an increased magnitude of negative $\overline{q}_\phi$ with the development of strong wind shear and diminished static stability near the subtropical mesospheric and polar jet cores (see Figure 6b). This development suggested a

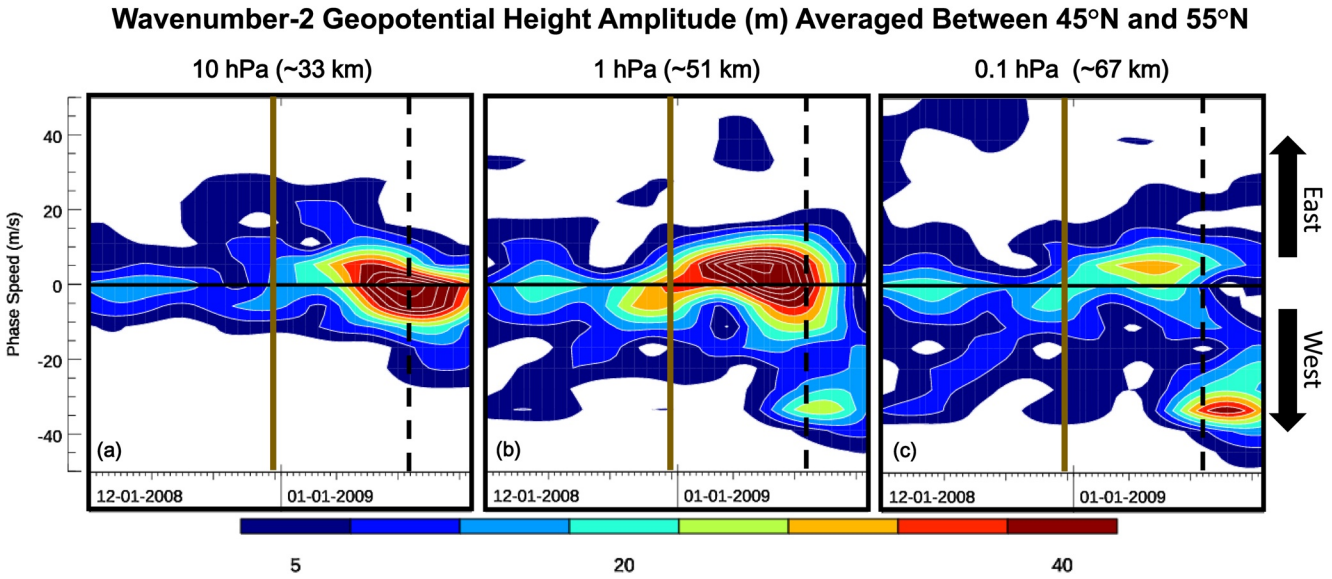

Figure 7. Zonal phase speed versus time plot of wavenumber-2 GHP amplitude (m) at 33, 51, and 67 km averaged between 45°N and 55°N. White contours increment by 5 m. Positive phase speed indicates eastward movement. The vertical brown line corresponds with the formation of a double-maxima wind structure on December 31, 2008. The vertical dashed line indicates SSW onset on January 22, 2009. GHP, geopotential height perturbation; SSW, sudden stratospheric warming.

strong destabilization of the background wind near the zero-wind line. Figure 8c shows that this growing instability had a wavenumber-2 pattern. Hence, the development and persistence of the double-maxima wind structure prior to SSW encouraged the *in situ* generation of a wavenumber-2 EPW leading up to SSW onset via shear instability.

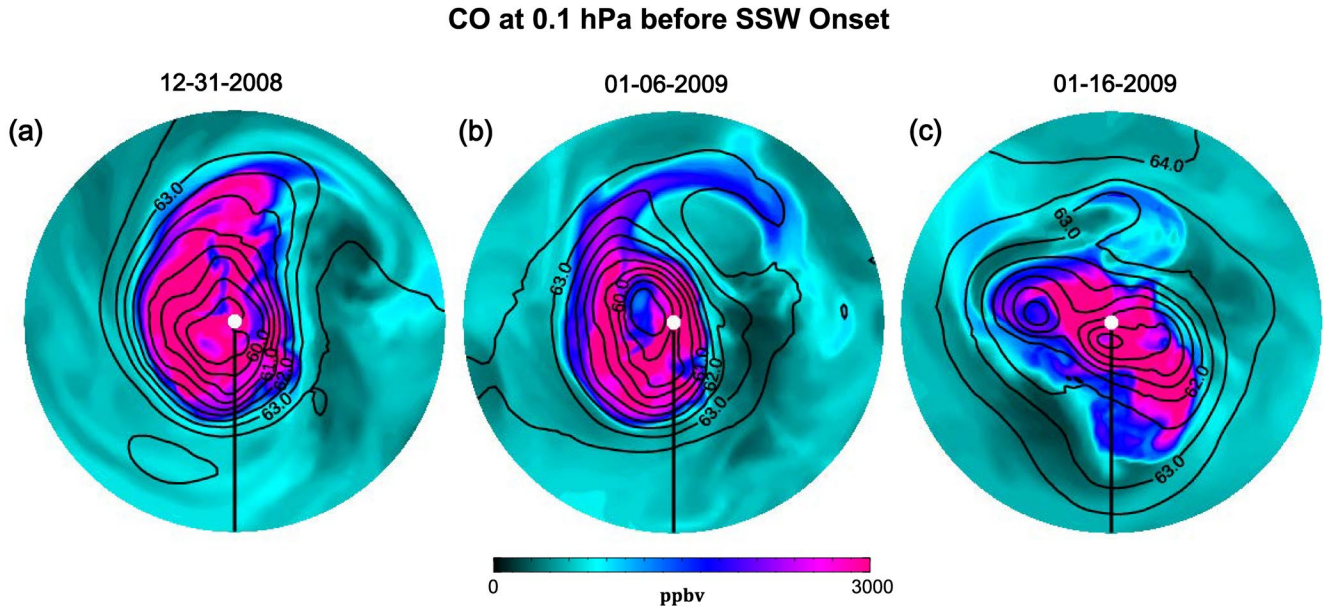

Figure 8. Stereographic polar projections extending from the pole to 10°N of carbon monoxide (CO) at 0.1 hPa. Geopotential height (black contours) is incremented by 0.5 km. The thick black vertical line depicts the Prime Meridian.

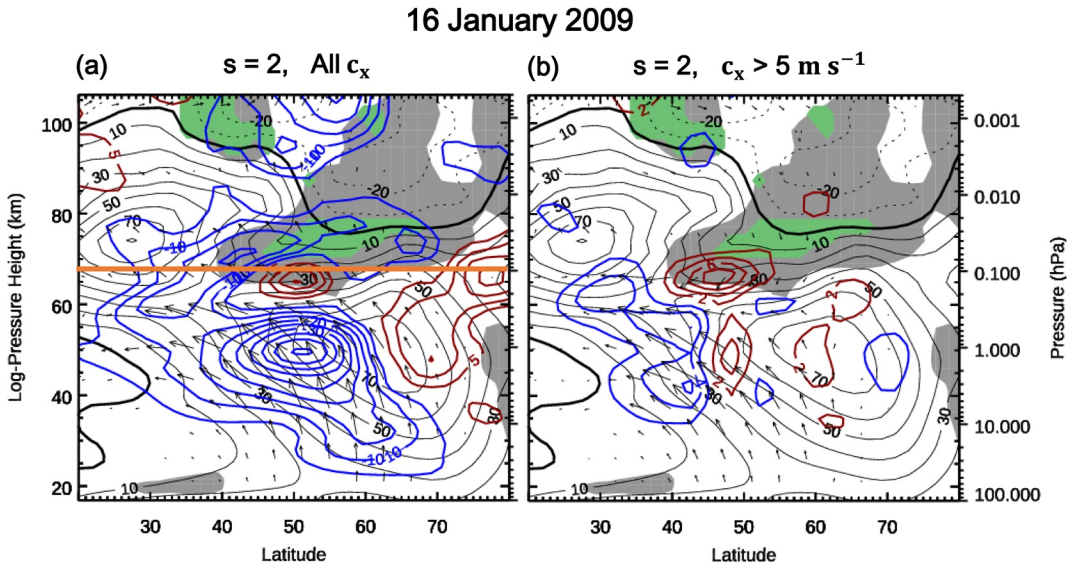

Figure 9. Altitude–latitude sections of PW2 EP flux and EP flux divergence for (a) all phase speeds and (b) eastward phase speeds. Negative (blue) and positive (red) EP flux divergence is contoured every (a) 5 m s^{-1} day^{-1} and (b) 2 m s^{-1} day^{-1}. Westward (dotted black contour) and eastward (solid thin black contour) wind increment by 10 m s^{-1}, with the zero-wind line thickened. The negative $\overline{q}_\phi$ region is gray shaded. The presence of a critical layer inside the negative $\overline{q}_\phi$ regions is shaded in green. The EP flux vector components are scaled as done in Figure 4, but the EPW2 vector magnitudes are multiplied by 10.0. PW2, wavenumber-2 planetary wave; EP, Eliassen-Palm; EPW, eastward-propagating planetary wave.

3.4. Generation of EPWs From Shear Instability

Figure 9a shows the EP flux for wavenumber-2 PWs (hereafter PW2s) of all phase speeds just prior to SSW onset (January 16, 2009). Here, the double-maxima wind structure persisted from its formation around December 31, 2008. An extensive region of negative $\overline{q}_\phi$ (gray-shaded area) remained in a meridional local minimum of $\overline{u}$ near 0.1 hPa. Consistent with the split polar vortex, PW2s dominated the wave field. Strong PW2 activity emanated upward from the troposphere and was refracted equatorward upon reaching the stratopause and above. Westward forcing (blue contours) associated with PW2s appeared mainly above and on the equatorward side of the polar jet. Its strong decelerative effects on $\overline{u}$ further allowed eastward GWD to reach the upper mesosphere as noted in Figure 4b.

We elucidate EPWs by band-pass filtering for wavenumber-2 disturbances with eastward phase speeds of 5 m s^{-1} and greater. We refer to the filtered result as EPW2. The selected phase speed range for filtering was based on the identified PW2 eastward peak in Figure 7. Considering the broad phase speed distribution shown in Figure 7, the band-passed EPW2 was a small contribution to the total PW2. Nevertheless, filtering should better illustrate the EPW characteristics by minimizing the influence from strong quasi-stationary PW activity, suggested by the phase speed distribution in Figure 7.

The resulting EPW2 EP flux is shown in Figure 9b. As noted by Coy et al. (2011), upward EPW2 originated from the troposphere. Upon reaching the stratopause, its flux convergence imposed westward forcing on the equatorward side of the polar jet. EPW2 activity also emanated from the bottom edge of the negative (gray) $\overline{q}_\phi$ region with an overlying critical layer (green shading). This emanation resulted in a strong EPW2 EP flux divergence (red contours) and overlapped with the midlatitude region of PW2 EP flux divergence in Figure 9a. Such overlapping highlights the dominance of EPW2 to the overall PW2 activity in that region. The collocation of a negative $\overline{q}_\phi$ region, a critical layer, and emerging EPW2 activity strongly suggests *in situ* EPW2 growth from shear instability. Occurring in the eastward flow regime, such growth indicates that these unstable waves had an eastward phase speed, as supported by the eastward shift in the phase speed distribution in Figure 7 around January 16. Comparing Figures 6c and 6f, the negative $\overline{q}_\phi$ region was dominated by the barotropic term (dark gray region) and baroclinic term (dark red region) on the equatorward and poleward side, respectively. Thus, the emanating EPW2 flux activity pointed equatorward as well

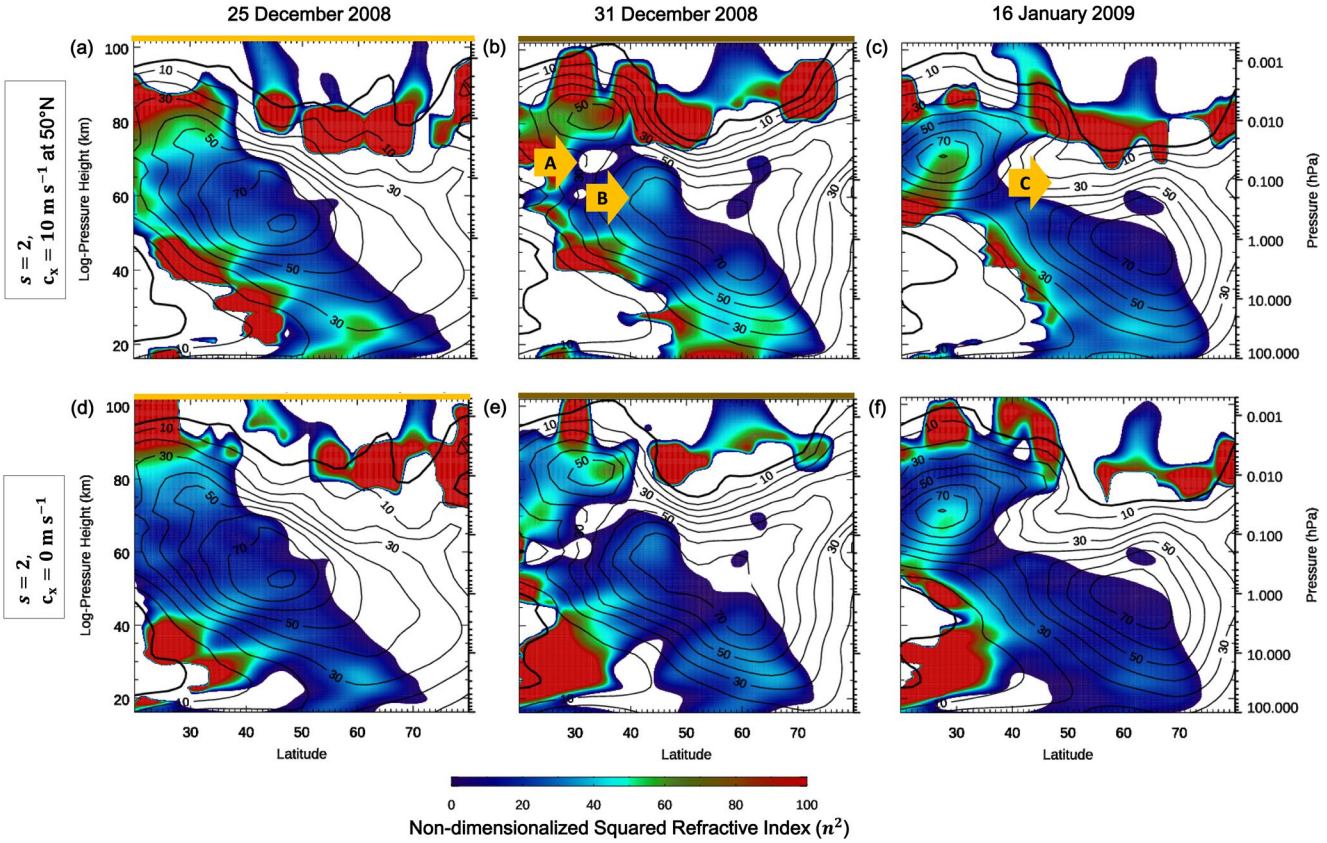

Figure 10. Nondimensionalized squared refractive index, $\boldsymbol{n^2}$ (color-filled contours) for (a–c) slow eastward and (d–f) stationary PW2s with specified frequencies labeled at the left of each row. Columns are organized by reference date. Eastward $\overline{u}$ is contoured every 10 m s^{-1} as thin black contours, with the zero-wind line thickened. Features A–C depict notable changes to the $\boldsymbol{n^2}$ field and are discussed in Sections 3.5 and 3.6. PW2, wavenumber-2 planetary wave.

as downward toward a flux convergence region in the subtropics, where it merged with the EPW2 activity from below. Overall, the characteristics of these unstable waves are consistent with EPW2 identified by Coy et al. (2011) and Iida et al. (2014).

3.5. Propagation of EPW2

We explore the linear propagation of EPW2 in Figure 10 based on the (nondimensionalized) squared refractive index ($\boldsymbol{n^2}$). As defined in Equation 2, $\boldsymbol{n^2}$ depends on N_B^2, $\overline{q}_\phi$, and the critical layer (via the quantity $\overline{u} - c_x$). In particular, $\boldsymbol{n^2}$ becomes negative when $\overline{q}_\phi$ is negative. It decreases with either decreasing N_B^2 or $\overline{q}_\phi$ and becomes infinite at the critical layer.

In Figure 10, we compute $\boldsymbol{n^2}$ for a stationary PW2 ($c_x = 0$) and for a PW2 with eastward phase speed of 10 m s^{-1} at 50°N. As noted in Figure 7, the phase speed of the emergent EPW2, after the formation of the double-maxima wind configuration, tended to focus around 5 m s^{-1}. However, given the broad phase speed distribution of PW2 perturbations, we used the phase speed of 10 m s^{-1} (at 50°N) in computing $\boldsymbol{n^2}$ to illustrate the upper bound characteristics of EPW2 propagation. The white areas in Figure 10 represent negative $\boldsymbol{n^2}$ values. Red regions correspond to extremely large $\boldsymbol{n^2}$ values (>100), often occurring near critical layers.

On December 25, a broad region of low (bluish) $\boldsymbol{n^2}$ tilted along with the eastward wind structure for both EPW2 (Figure 10a) and stationary PW2 (Figure 10d). EPW2 is expected to be weak above 10 hPa at this time (based on Figure 7) since any EPW2 propagation would tend to be refracted toward larger $\boldsymbol{n^2}$ values on the equatorward flank of the jet and dissipate near its critical layer. This propagational pattern would be similar for stationary PW2. With the formation of the double-maxima wind configuration on December 31, PW2

started to grow (as seen near the vertical brown line in Figure 7) throughout the stratosphere as n^2 drastically changed. The aforementioned valley of low $\overline{q}_\phi$ values (found in Figure 6b between the subtropical mesospheric and polar night jets) reduced n^2 around 30°N–40°N and 60–80 km, labeled as feature A. This tended to limit PW2 from propagating further upward and equatorward toward the subtropical mesospheric zero-wind line. Moreover, an enhanced positive $\overline{q}_\phi$ in Figure 6b corresponds to a localized region of large n^2 around at 44°N and 60 km, labeled as feature B. Taken together, changes in n^2 at features A and B established a waveguide that encouraged PW2s to propagate toward, but not beyond, the intervening region between the subtropical and polar jets. Correspondingly, strong PW EP flux convergence occurred (as evident in Figure 3b), indicating the dissipation of stationary PW2 and EPW2 at that location.

By January 16, EPW2 became very strong near the stratopause (see Figure 7). The northward migration of the polar jet increased the $\overline{u}$ curvature and increased $\overline{q}_\phi$, evidenced by the maxima in Figure 6c at 10 hPa and 70°N. This increased curvature was expected to also enhance n^2 values since n^2 depends on $\overline{q}_\phi$ through Equation 3. Consequently, comparing Figures 10a and 10c as well as Figures 10d and 10f, regions of positive n^2 spread toward higher latitudes between 10 and 0.1 hPa, allowing EPW2 and PW2 (originating in the midlatitude troposphere) to propagate more vertically along the edge of the polar vortex, as shown in Figure 9b. The predominantly vertical propagation of PWs prior to SSW onset is common (e.g., Limpasuvan et al., 2012).

3.6. Unstable EPW From an Overreflection Perspective

Unstable waves can manifest as overreflection and transmission as suggested by studies like Lindzen et al. (1980) and Harnik and Heifetz (2007). Illustrated in Figure 1, such a perspective links the influence of upward-propagating tropospheric EPW2 disturbances reported by Coy et al. (2011), to the production of mesospheric unstable waves during the 2009 SSW suggested by Iida et al. (2014). Since the vertical geometry for instability idealized in Figure 1 is homomorphic with the meridional geometry (Lindzen, 1988), a similar meridionally oriented geometry could also encourage overreflection. Hence, unlike the idealized scenario, the overreflected waves in reality can have both vertical and meridional components in their group velocity.

The illustration in Figure 1 bears a strong resemblance to Figure 9b. In particular, we see the upward propagation of EPW2 impinged on the bottom portion of the unstable (gray) region of negative $\overline{q}_\phi$. As diagnosed in Figure 10c, the waveguide (by January 16) readily allowed upward EPW2 activity to reach the unstable region, where the EPW2 critical layer (green region) resided. Downward EPW2 EP flux vectors point away from the unstable region in Figure 9b, leaving behind a strong region of EP flux divergence. The emergent EPW2 activity was below the wave evanescent region of negative n^2 values, as shown in the white region (labeled as feature C) in Figure 10c. As such, these vectors can be interpreted as the overreflection of upward-propagating EPW2. Overall, we expect the downward energy propagation to have been negated or masked by the persistent upward EPW2 activity from below. As noted above, given the complex nature of $\overline{q}_\phi$, the EPW2 activity emerging from the unstable region may also point equatorward.

Comparing Figures 10c and 10f, the evanescent region (feature C) was thinner for EPW2 than for PW2, suggesting that EPW2 was more conducive to overreflection since it would need to tunnel a shorter vertical distance to its critical layer (as suggested in Figure 1). Thus, there was a bias to produce unstable EPWs. After the formation of a double-maxima wind configuration, the poleward movement of the polar jet allowed PW2 and EPW2 to propagate vertically (discussed in Section 3.5), further thinning the evanescent region. The eastward bias in the resultant unstable wave production is shown by the eastward shift in GHP phase speed distribution in Figure 7.

Figure 11a illustrates the altitude–time evolution of the vertical component of EPW2 EP flux, averaged from 45°N to 55°N. The upward flux is shown in brownish filled contours and downward in bluish filled contours. Following the formation of a double-maxima wind configuration on December 31 (brown vertical line), EPW2 propagated from the surface up to the stratopause. Upon reaching the bottom of the unstable region (black stipples) in which a critical layer (green stipples) resides, overreflection occurred as evidenced by the negative (bluish areas) EP flux near 60 km and around January 3. There, EP flux divergence (red contours) imposed an eastward forcing of 4 m s^{-1} day^{-1}. Around January 10, another stronger episode of

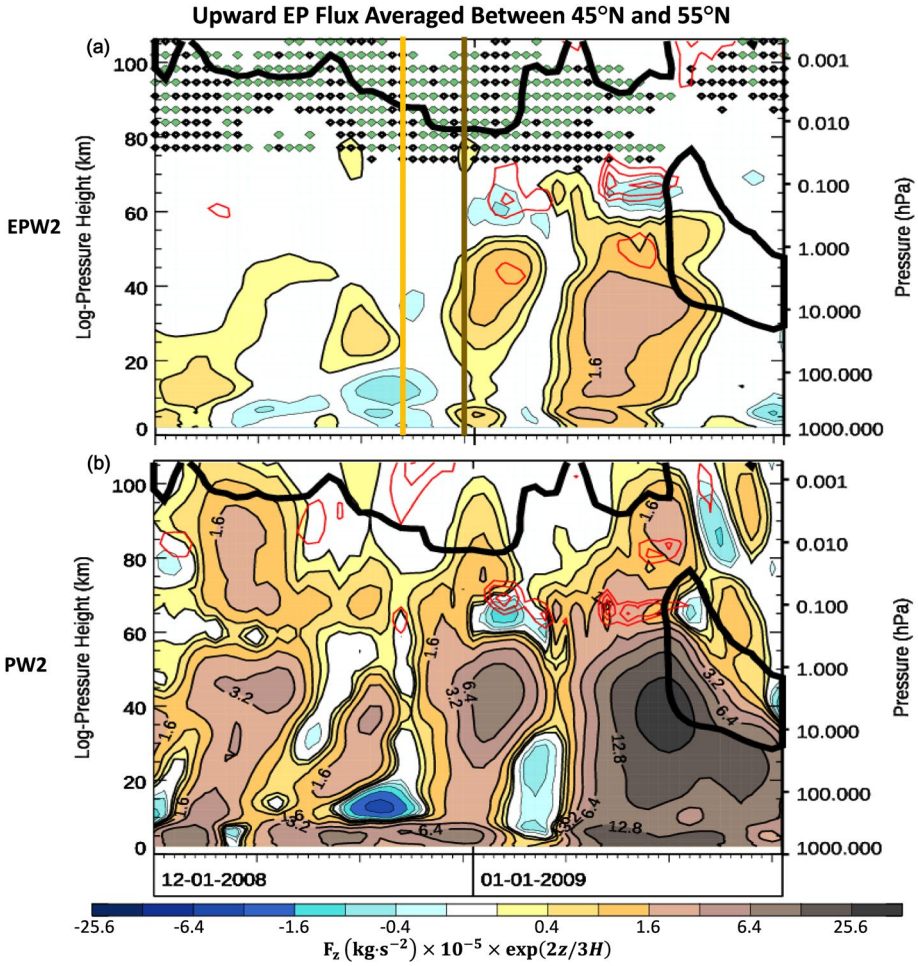

Figure 11. Altitude–time section of PW2 vertical EP flux (filled contours) for waves of (a) eastward phase speeds greater than 5 m s^{-1} and (b) all phase speeds. Upward (downward) fluxes are indicated by brown (blue) shaded contours of $+(-)\,0.2 \times 2^m$ kg s^{-2}, $m \in [1,2,3,4,5,6,7,8]$. Red contours show EP flux divergence and are incremented by (a) 2 m s^{-1} day^{-1} and (b) 5 m s^{-1} day^{-1}. Thick black contour depicts the zero-wind line. Locations with negative $\overline{q}_\phi$ are marked by black stipples. Locations where a critical layer exists inside a region of negative $\overline{q}_\phi$ are marked by green stipples. Stippled regions shown in (a) also apply to (b). Latitudinal averaging is between 45°N and 55°N. PW2, wavenumber-2 planetary wave; EP, Eliassen-Palm.

upward EPW2 emerged from the surface. Like the earlier episode, we see overreflection from the unstable region and strong EP flux divergence just before the wind reversal as marked by the zero-wind line (thickened black contour). Coy et al. (2011) reported similar bursts of PW2 signal originating near the surface that reached 1 hPa within days to weeks. Overall, these overreflection characteristics are consistent with features illustrated in Figure 9b.

The evolution of EP Flux for all PW2 is shown in Figure 11b. In comparison to Figure 11a, the EPW2 flux comprised some of the persistent upward PW2 bursts, especially after December 31. In reference to Figure 1, wave transmission could appear in the positive $\boldsymbol{n^2}$ region above the evanescent region. From Figure 10c, this evanescent region (near feature C) is roughly 20 km thick. Transmitted waves propagating from the critical layer can readily deposit their momentum creating a region of EP flux convergence (westward acceleration). This pattern is evident in Figure 9a as a region of PW2 EP flux convergence (blue contours) that sits atop a region of EP flux divergence (red contours) in the unstable (gray) region. Additional evidence of transmission also appears in Figure 11b with upward PW2 flux (brown region) above the region of downward flux (blue shading) along with EP flux divergence (red contours).

4. Summary

The anomalous growth of the mesospheric EPWs with a zonal phase speed of ~10 m s^{-1} prior to the 2009 split SSW was identified in this paper, in agreement with past studies (e.g., Coy et al., 2011; Iida et al., 2014; Song et al., 2020). Our diagnoses reveal new key insights about these precursory EPWs. Namely,

(1) They arise from shear instability in the mesosphere via wave overreflection.
(2) Created by GW and PW forcing ~20 days before SSW onset, the unstable flow is characterized by a double-maxima wind structure with a subtropical mesospheric core and polar stratospheric core.
(3) This wind configuration sets up a unique wave geometry that, from an overreflection perspective, favors the production of eastward-propagating PWs.

Preceding the formation of the double-maxima wind configuration was the presence of subtropical eastward GWD adjacent to the midlatitude to high-latitude westward GWD in the mesosphere. This distinctive GWD pattern induced a subtropical upwelling that locally lowered static stability and, consequently, altered the refractive index. Changes in wave propagation led to enhanced PW damping near the intervening region between the wind maxima, further promoting the jet separation. Thus, a positive feedback loop was created in which the double-maxima wind configuration was sustained, while the mesospheric flow became more susceptible to shear instability. With the formation of a double-maxima wind structure, the polar jet core strengthened and migrated poleward as the wave evanescent layer in the unstable region became thinner. The northward-shifted polar jet also guided the upward-propagating PWs more vertically toward the thinning evanescent region (see Figures 6 and 10). The vertical orientation increased the likelihood of overreflection, particularly for EPWs. The poleward migration of the polar night jet may likewise provide the background conditions that favor SSW onset through resonance (e.g., Albers & Birner, 2014).

The background flow evolution leading into the January 2009 SSW supported a wave geometry suitable for wave overreflection (cf., Figure 1). As a result, PWs with eastward phase speeds were generated near the stratopause from instability. A composite study by Domeisen et al. (2018) found a tendency for an eastward shift in the PW zonal phase speed distribution with altitude prior to SSW onset. These authors also noted that PWs propagating upward into the stratosphere are limited to low wavenumbers by the strong wintertime stratospheric background wind exceeding a critical speed. Since the critical speed of the background wind is relative to the wave, eastward-propagating (westward-propagating) waves experience a higher (lower) critical speed. Thus, eastward-propagating waves would be able to propagate into stronger stratospheric winds, with a larger effect at higher wavenumbers. However, overreflection also generates PWs with a bias toward eastward phase speeds (discussed in Section 3.6). This suggests a possible compounding effect that would shift PWs in the stratosphere toward eastward phase speeds, particularly for split SSWs.

In examining other SSW events (not shown), we found that the generation of EPWs was common prior to SSW onset and was commonly associated with a double-maxima wind configuration, formed at different times with respect to SSW onset. Overall, EPWs could significantly impact the mesospheric wind structure and play a key role in the nature and timing of SSW events. In particular, EPWs help reduce the preexisting wind shear and, thereby, stabilize the polar vortex. GWD may likewise generate a nonconservative wave source for EPWs (Song et al., 2020) and work in tandem with $\overline{q}_\phi$ reversal in generating *in situ* EPWs. Further research is needed to understand the source mechanisms of *in situ* wave generation in the mesosphere. The overreflection perspective offers a framework to connect variability in the stratosphere to stability in the mesosphere.

Acknowledgments
C.T.R. is supported by funding from the National Science Foundation (NSF) awards (RUI 1642232 and REU 1560210). V.L. is supported by NSF Intergovernmental Panel Agreement. The authors acknowledge the computing and technical support from the NCAR Computation Information Systems Laboratory as well as the Coastal Carolina University cyberinfrastructure (CCU CI) project, funded in part by NSF award MRI 1624068. The authors are indebted to the anonymous reviewers who have greatly improved this manuscript from the initial draft to its final stage.

Data Availability Statement

The relevant daily model output can be accessed through the CCU CI at https://mirror.coastal.edu/sce.

References

Albers, J. R., & Birner, T. (2014). Vortex preconditioning due to planetary and gravity waves prior to sudden stratospheric warmings. *Journal of the Atmospheric Sciences*, *71*, 4028–4054. https://doi.org/10.1175/JAS-D-14-0026.1

Andrews, D. G., Holton, J. R., & Leovy, C. B. (1987). *Middle atmosphere dynamics*. Academic Press.

Baldwin, M. P., & Dunkerton, T. J. (2001). Stratospheric harbingers of anomalous weather regimes. *Science*, *294*, 581–584. https://doi.org/10.1126/science.1063315

Butler, A. H., Seidel, D. J., Hardiman, S. C., Butchart, N., Birner, T., & Match, A. (2015). Defining sudden stratospheric warmings. *Bulletin of the American Meteorological Society*, *96*, 1913–1928. https://doi.org/10.1175/BAMS-D-13-00173.1

Charney, J. G., & Eliassen, A. (1949). A numerical method for predicting the perturbations of the middle latitude westerlies. *Tellus*, *1*, 38–54. https://doi.org/10.3402/tellusa.v1i2.8500

Coy, L., Eckermann, S. D., Hoppel, K. W., & Sassi, F. (2011). Mesospheric precursors to the major stratospheric sudden warming of 2009: Validation and dynamical attribution using a ground-to-edge-of-space data assimilation system. *Journal of Advances in Modeling Earth Systems*, *3*, M10002. https://doi.org/10.1029/2011MS000067

De Wit, R. J., Hibbins, R. E., Espy, P. J., Orsolini, Y. J., Limpasuvan, V., & Kinnison, D. E. (2014). Observations of gravity wave forcing of the mesopause region during the January 2013 major sudden stratospheric warming. *Geophysical Research Letters*, *41*, 4745–4752. https://doi.org/10.1002/2014GL060501

Dickinson, R. E. (1973). Baroclinic instability of an unbounded zonal shear flow in a compressible atmosphere. *Journal of the Atmospheric Sciences*, *30*, 1520–1527.

Domeisen, D. I. V., Martius, O., & Jiménez-Esteve, B. (2018). Rossby wave propagation into the Northern Hemisphere stratosphere: The role of zonal phase speed. *Geophysical Research Letters*, *45*, 2064–2071. https://doi.org/10.1002/2017GL076886

Duck, T. J., Whiteway, J. A., & Carswell, A. I. (2001). The gravity wave–Arctic stratospheric vortex interaction. *Journal of the Atmospheric Sciences*, *58*(23), 3581–3596. https://doi.org/10.1175/1520-0469(2001)058<3581:TGWASV>2.0.CO;2

Fetzer, E. J., & Gille, J. C. (1994). Gravity wave variance in LIMS temperatures. Part I: Variability and comparison with background winds. *Journal of the Atmospheric Sciences*, *51*(17), 2461–2483. https://doi.org/10.1175/1520-0469(1994)051<2461:GWVILT>2.0.CO;2

Gelaro, R., McCarty, W., Suárez, M. J., Todling, R., Molod, A., Takacs, L., et al. (2017). The modern-era retrospective analysis for research and applications, version 2 (MERRA-2). *Journal of Climate*, *30*, 5419–5454. https://doi.org/10.1175/JCLI-D-16-0758.1

Goncharenko, L. P., Chau, J. L., Liu, H.-L., & Coster, A. J. (2010). Unexpected connections between the stratosphere and ionosphere. *Geophysical Research Letters*, *37*, L10101. https://doi.org/10.1029/2010GL043125

Harada, Y., Goto, A., Hasegawa, H., Fujikawa, N., Naoe, H., & Hirooka, T. (2010). A major stratospheric sudden warming event in January 2009. *Journal of the Atmospheric Sciences*, *67*, 2052–2069. https://doi.org/10.1175/2009JAS3320.1

Harnik, N., & Heifetz, E. (2007). Relating overreflection and wave geometry to the counterpropagating Rossby wave perspective: Toward a deeper mechanistic understanding of shear instability. *Journal of the Atmospheric Sciences*, *64*(7), 2238–2261. https://doi.org/10.1175/JAS3944.1

Hartmann, D. L. (1983). Barotropic instability of the polar night jet stream. *Journal of the Atmospheric Sciences*, *40*(4), 817–835. https://doi.org/10.1175/1520-0469(1983)040<0817:BIOTPN>2.0.CO;2

Hitchman, M. H., Gille, J. C., Rodgers, C. D., & Brasseur, G. (1989). The separated polar winter stratopause: A gravity wave driven climatological feature. *Journal of the Atmospheric Sciences*, *46*(3), 410–422. https://doi.org/10.1175/1520-0469(1989)046<0410:TSPWSA>2.0.CO;2

Iida, C., Hirooka, T., & Eguchi, N. (2014). Circulation changes in the stratosphere and mesosphere during the stratospheric sudden warming event in January 2009. *Journal of Geophysical Research: Atmospheres*, *119*, 7104–7115. https://doi.org/10.1002/2013JD021252

Leovy, C. (1964). Simple models of thermally driven mesopheric circulation. *Journal of the Atmospheric Sciences*, *21*(4), 327–341.

Leovy, C. B., & Webster, P. J. (1976). Stratospheric long waves: Comparison of thermal structure in the Northern and Southern Hemispheres. *Journal of the Atmospheric Sciences*, *33*, 1624–1638. https://doi.org/10.1175/1520-0469(1976)033<1624:SLWCOT>2.0.CO;2

Limpasuvan, V., Orsolini, Y. J., Chandran, A., Garcia, R. R., & Smith, A. K. (2016). On the composite response of the MLT to major sudden stratospheric warming events with elevated stratopause. *Journal of Geophysical Research: Atmospheres*, *121*, 4518–4537. https://doi.org/10.1002/2015JD024401

Limpasuvan, V., Richter, J. H., Orsolini, Y. J., Stordal, F., & Kvissel, O.-K. (2012). The roles of planetary and gravity waves during a major stratospheric sudden warming as characterized in WACCM. *Journal of Atmospheric and Solar-Terrestrial Physics*, *78–79*, 84–98. https://doi.org/10.1016/j.jastp.2011.03.004

Lindzen, R. S. (1988). Instability of plane parallel shear flow (toward a mechanistic picture of how it works). *Pure and Applied Geophysics*, *126*(1), 103–121.

Lindzen, R. S., Farrell, B., & Tung, K.-K. (1980). The concept of wave overreflection and its application to baroclinic instability. *Journal of the Atmospheric Sciences*, *37*, 44–63. https://doi.org/10.1175/1520-0469(1980)037<0044:TCOWOA>2.0.CO;2

Manney, G. L., Krüger, K., Pawson, S., Minschwaner, K., Schwartz, M. J., Daffer, W. H., et al. (2008). The evolution of the stratopause during the 2006 major warming: Satellite data and assimilated meteorological analyses. *Journal of Geophysical Research*, *113*, D11115. https://doi.org/10.1029/2007JD009097

Manney, G. L., Nathan, T. R., & Stanford, J. L. (1988). Barotropic stability of realistic stratospheric jets. *Journal of the Atmospheric Sciences*, *45*(18), 2545–2555.

Marsh, D. R., Mills, M. J., Kinnison, D. E., Lamarque, J.-F., Calvo, N., & Polvani, L. M. (2013). Climate change from 1850 to 2005 simulated in CESM1(WACCM). *Journal of Climate*, *26*, 7372–7391. https://doi.org/10.1175/JCLI-D-12-00558.1

Matsuno, T. (1971). *A dynamical model of stratospheric sudden warming, 1479–1494*. Retrieved from http://journals.ametsoc.org/doi/pdf/10.1175/1520-0469%281971%29028%3C1479%3AADMOTS%3E2.0.CO%3B2

Matthias, V., & Ern, M. (2018). On the origin of the mesospheric quasi-stationary planetary waves in the unusual Arctic winter 2015/2016. *Atmospheric Chemistry and Physics*, *18*(7), 4803–4815. https://doi.org/10.5194/acp-18-4803-2018

O'Neill, A., & Youngblut, C. E. (1982). Stratospheric warmings diagnosed using the transformed Eulerian-mean equations and the effect of the mean state on wave propagation. *Journal of the Atmospheric Sciences*, *39*, 1370–1386. https://doi.org/10.1175/1520-0469(1982)039<1370:SWDUTT>2.0.CO;2

Orsolini, Y., & Simon, P. (1995). Idealized life cycles of planetary-scale barotropic waves in the middle atmosphere. *Journal of the Atmospheric Sciences*, *52*(22), 3817–3835. https://doi.org/10.1175/1520-0469(1995)052<3817:ILCOPS>2.0.CO;2

Pedatella, N. M., Oberheide, J., Sutton, E. K., Liu, H. L., Anderson, J. L., & Raeder, K. (2016). Short-term nonmigrating tide variability in the mesosphere, thermosphere, and ionosphere. *Journal of Geophysical Research: Space Physics*, *121*, 3621–3633. https://doi.org/10.1002/2016JA022528

Pedlosky, J. (1987). *Geophysical fluid dynamics* (2nd ed.). Springer.

Richter, J. H., Sassi, F., & Garcia, R. R. (2010). Toward a physically based gravity wave source parameterization in a general circulation model. *Journal of the Atmospheric Sciences*, *67*, 136–156. https://doi.org/10.1175/2009JAS3112.1

Salby, M. L. (1996). *Fundamentals of atmospheric physics*. Academic Press.

Sassi, F., Liu, H. L., & Emmert, J. T. (2016). Traveling planetary-scale waves in the lower thermosphere: Effects on neutral density and composition during solar minimum conditions. *Journal of Geophysical Research: Space Physics*, *121*, 1780–1801. https://doi.org/10.1002/2015JA022082

Sato, K., & Nomoto, M. (2015). Gravity wave-induced anomalous potential vorticity gradient generating planetary waves in the winter mesosphere. *Journal of the Atmospheric Sciences*, *72*, 3609–3624. https://doi.org/10.1175/JAS-D-15-0046.1

Smagorinsky, J. (1953). The dynamical influence of large-scale heat sources and sinks on the quasi-stationary mean motions of the atmosphere. *Quarterly Journal of the Royal Meteorological Society*, *79*, 342–366.

Solomon, S., Garcia, R. R., Olivero, J. J., Bevilacqua, R. M., Schwartz, P. R., Clancy, R. T., & Muhleman, D. O. (1985). Photochemistry and transport of carbon monoxide in the middle atmosphere. *Journal of the Atmospheric Sciences*, *42*(10), 1072–1083.

Song, B.-G., Chun, H.-Y., & Song, I.-S. (2020). Role of gravity waves in a vortex-split sudden stratospheric warming in January 2009. *Journal of the Atmospheric Sciences*, *77*, 3321–3342. https://doi.org/10.1175/JAS-D-20-0039.1

Zhang, J., Limpasuvan, V., Orsolini, Y. J., Espy, P. J., & Hibbins, R. E. (2021). Climatological westward-propagating semidiurnal tides and their composite response to sudden stratospheric warmings in SuperDARN and SD-WACCM-X. *Journal of Geophysical Research: Atmospheres*, *126*, e2020JD032895. https://doi.org/10.1029/2020JD032895